




## Transport of an intense proton beam from a cone-structured target through plastic foam with unique proton source modeling

K. Bhutwala <sup>1,\*</sup> C. McGuffey <sup>1,4</sup> W. Theobald,<sup>2</sup> O. Deppert,<sup>3</sup> J. Kim,<sup>1</sup> P. M. Nilson,<sup>2</sup> M. S. Wei,<sup>4,†</sup> Y. Ping,<sup>5</sup> M. E. Foord,<sup>5</sup> H. S. McLean <sup>5</sup> P. K. Patel,<sup>5</sup> A. Higginson,<sup>1,‡</sup> M. Roth,<sup>3</sup> and F. N. Beg<sup>1</sup>

<sup>1</sup>Center for Energy Research, University of California, San Diego, La Jolla, California 92093-0417, USA

<sup>2</sup>Laboratory for Laser Energetics, University of Rochester, Rochester, New York 14623, USA

<sup>3</sup>Institut für Kernphysik, Technische Universität Darmstadt, 64289 Darmstadt, Germany

<sup>4</sup>General Atomics, P.O. Box 85608, San Diego, California 92186-5608, USA

<sup>5</sup>Lawrence Livermore National Laboratory, P.O. Box 808, Livermore, California 94550, USA



(Received 25 October 2021; accepted 31 March 2022; published 13 May 2022)

Laser-accelerated proton beams are applicable to several research areas within high-energy density science, including warm dense matter generation, proton radiography, and inertial confinement fusion, which all involve transport of the beam through matter. We report on experimental measurements of intense proton beam transport through plastic foam blocks. The intense proton beam was accelerated by the 10 ps, 700 J OMEGA EP laser irradiating a curved foil target, and focused by an attached hollow cone. The protons then entered the foam block of density 0.38 g/cm<sup>3</sup> and thickness 0.55 or 1.00 mm. At the rear of the foam block, a Cu layer revealed the cross section of the intense beam via proton- and hot electron-induced Cu-K<sub>α</sub> emission. Images of x-ray emission show a bright spot on the rear Cu film indicative of a forward-directed beam without major breakup. 2D fluid-PIC simulations of the transport were conducted using a unique multi-injection source model incorporating energy-dependent beam divergence. Along with postprocessed calculations of the Cu – K<sub>α</sub> emission profile, simulations showed that protons retain their ballistic transport through the foam and are able to heat the foam up to several keV in temperature. The total experimental emission profile for the 1.0 mm foam agrees qualitatively with the simulated profile, suggesting that the protons indeed retain their beamlike qualities.

DOI: [10.1103/PhysRevE.105.055206](https://doi.org/10.1103/PhysRevE.105.055206)

### I. INTRODUCTION

It is well-known that the irradiation of thin foil targets by high intensity ( $\gg 10^{18}$  W/cm<sup>2</sup>), short-pulse (0.01 – 10 ps) lasers generates laminar proton beams with MeV energies and extreme current densities [1]. Beam parameters typical at present include proton energies up to 100 MeV and current densities up to  $\sim 10^9$  A/cm<sup>2</sup>. The advantage of these laser-accelerated proton beams lies in their short bunch duration, typically on the order of the laser pulse duration ( $\sim$ ps) at their source, and 100 ps or less as they disperse over mm distances. Combined with their favorable deposition characteristics, this makes them particularly effectual in isochoric heating of thin foils to warm dense regimes [2–7], proton radiography of rapidly evolving high-energy density plasmas [8–10], and the proton fast ignition (FI) scheme of inertial confinement fusion [11,12].

Although the various mechanisms of laser-driven proton acceleration have been and continue to be well-studied, the transport and heating capabilities of these intense proton

beams through low-density plasma is not. Ultralow density plastic foams which, when heated to high temperatures, can reasonably stand in for low-density plasma have become available, opening this field of research to the laboratory setting. Proton heating has recently been used to create warm dense carbon from plastic foams [13], offering equation-of-state studies of these complex regimes. Proton heating could also facilitate the study of low-rate nuclear reactions in astrophysical objects with near-solid density and keV temperatures [14]. Following the simulation work on the dynamics of intense beam transport in solids [15], investigating how proton heating and transport change in low-density foams are of great interest in their own right.

When short-pulse laser-accelerated laminar proton beams were discovered and attributed to target normal sheath acceleration (TNSA [1,16]), they were also immediately recognized as a viable charged particle beam for FI. Protons' large inertia (compared to electrons) makes them less susceptible to electromagnetic fields present in the coronal plasma outside the compressed core, thereby mitigating transport instabilities that plague electron FI [17,18]. Energetic protons also exhibit a Bragg peak in energy deposition, which means the majority of a proton's energy is deposited near their stopping range. Crucially, since laser-accelerated proton beams have a broadband energy spectrum, the high-energy protons arrive at and heat the DT capsule, which (depending on material characteristics) may extend

\*Corresponding author: kbhutwal@eng.ucsd.edu

†Present address: Laboratory for Laser Energetics, University of Rochester, Rochester, New York 14623, USA.

‡Present address: Colorado State University, Fort Collins, Colorado 80523, USA.

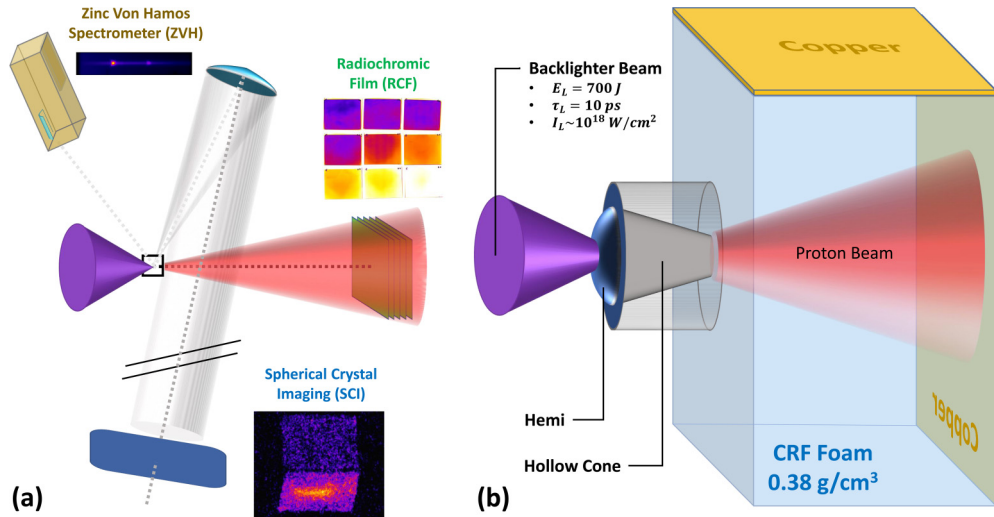


FIG. 1. (a) Experimental setup, wherein the OMEGA EP short-pulse laser (purple) irradiates the target structure. The resulting beams are characterized by the RCF pack, while the transport interaction is captured by the SCI and ZVH, all lying within several degrees of a plane (of the page). The target structure within the black square is magnified in (b). The foam block had a depth of either  $550\ \mu\text{m}$  or  $1000\ \mu\text{m}$  and was plated with  $10\text{-}\mu\text{m}$ -thick copper on the top and rear faces.

the stopping range of lower-energy protons [19] arriving later.

Proton FI has been explored in-depth [11,12], and the proton beam requirements to reach ignition have been evaluated numerically [20,21]. However, strong assumptions on transport through the coronal plasma near the cone tip to the compressed core are made in the rigid beam models applied. A study of beam transport in FI with an accurate accounting of beam divergence, which is known to depend on proton energy, has not been presented. Characterizing the transport of proton beams with energy tens of kJ in these conditions will be necessary for proton FI. Resistive magnetic fields have already been shown to collimate hot electron beams with high current densities ( $10^{11}\ \text{A}/\text{cm}^2$ ) within carbon samples [22]. In ultralow density gas jet targets, collective effects significantly alter the scattering of ion beams [23]. Simulations have shown that simultaneous heating and self-generated fields have a significant effect on the transport of proton beams with intensity  $\gg 10^9\ \text{A}/\text{cm}^2$  [15].

Here, we present an experimental study on transport of intense laser-driven protons in low-density plastic foams and show a modeling approach using 2D hybrid-PIC simulations. The experiment evaluated the transport of laser-accelerated cone-focused proton beams through low-density foam blocks by measuring the beam cross section at different depths. In Sec. II, the experimental results are presented, including measurements of the proton spectra from different target types. X-ray emission images are also presented, which provide evidence that the protons are still beamlike when they reach the back layer of the target. In Sec. III, we provide simulations of transport in the foam and postprocessing to validate the experimental x-ray images. We present a unique approach to modeling the proton beam source, taking into account the energy-dependent divergence of typical TNSA proton beams. By postprocessing the simulated particle information, we produce synthetic x-ray emission profiles and compare them to the experimental measurements.

## II. EXPERIMENTAL SETUP AND RESULTS

The experiment was carried out at the OMEGA EP facility, where a backlighter beam of energy 700 J, pulse length 10 ps, and intensity  $10^{18}\ \text{W}/\text{cm}^2$  irradiated a hemispherical cap (hemi) attached to a hollowed cone structure, accelerating and focusing protons through the cone tip and into a carbonized resorcinol-formaldehyde (CRF) foam block of density  $0.38\ \text{g}/\text{cm}^3$ . The diamondlike carbon hemi and cone opening were glued together and flushed (diameter  $300\ \mu\text{m}$ , also the hemi's radius of curvature). The cone length was  $300\ \mu\text{m}$  and had far-field tip diameter  $200\ \mu\text{m}$ . The far-field cone bulk surface was also glued to the foam. The foam block was  $1.0 \times 1.5\ \text{mm}$  in the laser-facing dimensions, with depths of either  $0.55\ \text{mm}$  or  $1.0\ \text{mm}$  to reveal the proton beam profile. CRF foam was chosen for its low density and therefore low proton stopping and scattering to elucidate the transport of protons. Cu foils  $10\ \mu\text{m}$  thick were glued onto the top and rear faces of the foam block to act as tracer layers that give a plane Cu- $K_\alpha$  emission for the visualization of energetic electrons and protons. The experimental setup is shown in Fig. 1.

### A. Radiochromic film diagnostic

Radiochromic film (RCF) packs were fielded on this experiment to diagnose the proton beams' spatial profiles and spectra. RCF darkens as a result of energy deposition, and dose measurements can be extracted from the darkening of the films [24]. A pack of  $6.35\ \text{cm}$  square films was placed  $16\ \text{cm}$  behind the target opposite the hemi structures, i.e., directly facing the rear Cu foil, if present, on every shot. Each successive layer of RCF in the pack marks an increasing penetration energy required by protons to reach that film. A pack contained 13 aluminum filters interleaved with ten films of type HD-v2 and 2 of type MD-55; the films' penetration energies spanned  $3.5 - 60\ \text{MeV}$ . Monte Carlo calculations of proton energy deposition in the film pack were convolved with

guesses of the energy distribution (an exponential spectrum capped below 0.5 MeV) for comparison to the measured doses using the approach described in Ref. [25]. The particle count and temperature of the proton distribution were varied to determine the best-fit spectrum through a residual minimizing routine utilizing the dose on films 2–10 or through the last film with measurable dose. The beam energy incident on the film is found by integrating the best-fit spectrum.

**B. X-ray diagnostics**

The spherical crystal imager (SCI) [26] was the primary diagnostic to visualize the Cu- $K_{\alpha}$  emission from energetic electron and proton collisions with Cu K-shell electrons. The imaging system comprises a spherically bent concave quartz crystal above the foam block  $27^{\circ}$  from the zenith and 276 mm away, and an image plate detector  $\sim 2.4$  m from the foam block in the opposite direction. The crystal refocuses incoming  $8048 \pm 6$  eV photons from the target onto the image plate.

The zinc von Hamos (ZVH) spectrometer was also used in this experiment to capture the time-integrated x-ray emission spectrum from various targets. This spectrometer contains a Highly-Ordered Pyrolytic Graphite (HOPG) crystal cylindrically bent along the nondispersive axis, thereby focusing 7–10 keV x-ray emission in first order along one dimension. The spectrometer was calibrated for the Cu- $K_{\alpha}$  emission by comparing the measured signal on image plates with an absolutely calibrated single-photon counting camera [27]. The ZVH viewed the target from above the laser axis.

**C. Experimental results**

Figure 2 shows the proton beam characteristics derived from the RCF data from targets with varying additional components, from a simple hemi to a hemi-cone target to a hemi-cone-foam package. The cone affects beam generation in two ways. On the one hand, hot electrons are able to escape from the hemi and into the cone structure, establishing a sheath field along the cone’s inner surface, which has been shown to focus the protons [7]. On the other hand, this migration leaves fewer electrons reverting back into the hemi and sustaining the electrostatic field to accelerate protons from the rear hemi surface. This results in better proton focusing at the cost of total proton beam energy. The latter affect can be seen in Fig. 2(b), where there is a factor of 2 decrease in both beam temperature and energy in going from a hemi-only to hemi-cone structure. Similarly, there is a decrease in the maximum proton energy from hemi-only (42 MeV detected) to hemi-cone (28 MeV detected) structure, shown in Fig. 2(a). When adding 0.55-mm- and 1-mm-thick foams, the total beam energy continues to decrease due to proton stopping, while the beam temperature does not change significantly from 6 MeV. The dynamics of ion acceleration with these structures are studied experimentally, theoretically, and computationally in Refs. [28,29].

Figures 3(a) and 3(b) depict the experimental cross-sectional view of the proton- and electron-induced Cu- $K_{\alpha}$  emission from two foam length cases. A raw SCI image is shown inset in Fig. 1(a), but here we have separated the top and rear portions and stretch them to account for the

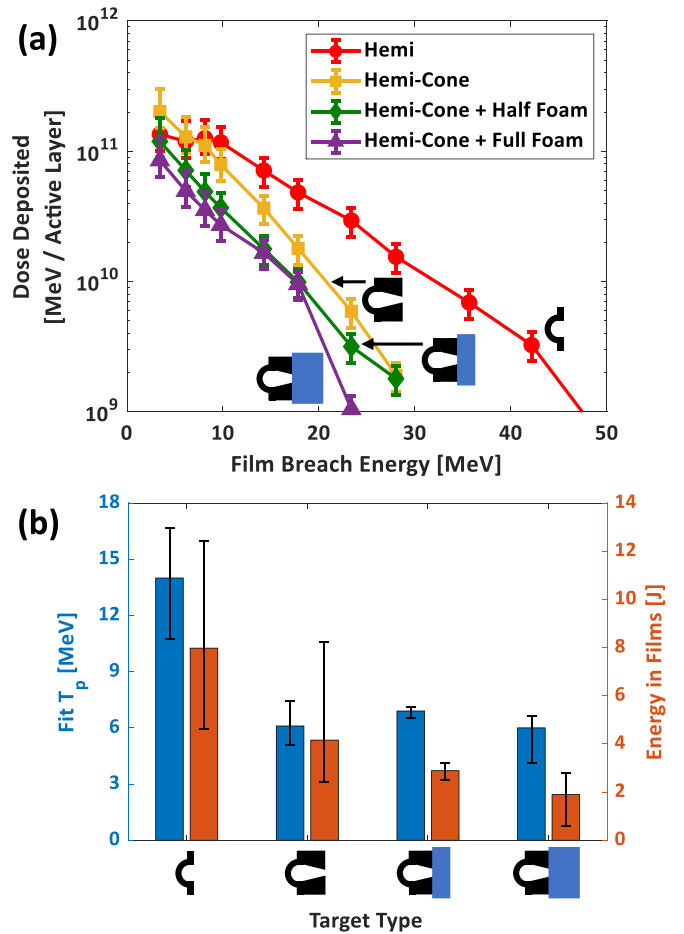


FIG. 2. Proton beam information derived from the RCF data. (a) The dose received by films versus film breach energy from hemi source foils with various attached structures. (b) Comparison [using data in (a)] of beam characteristic temperature and total energy through the film solid angle from each target type. Note that the films subtended the full beam so the energy (right bars, right axis) is less than the full beam energy, as discussed in the text.

viewing angle  $63^{\circ}$  above the equatorial plane. The top foils exhibit a relatively uniform emission, while the rear foils exhibit a brighter emission in a centralized spot, indicative of a forward-propagating particle beam, likely energetic protons. The size of the central bright spot corresponds to  $<20^{\circ}$  cone angle from the hemi apex, much narrower than would be expected from a beam of hot electrons [17], which typically exhibits substantial scattering and divergence within materials. This suggests that protons retain their beamlike qualities within the foam, and the spatial continuity of their intensities suggests little or no breakup of a proton beam. The experimental x-ray beam profiles were analyzed by radially binning and summing the signal to yield an experimental profile of  $dY_{K_{\alpha}}/dAd\Omega$ . Simulations of protons and hot electrons are explored in Sec. III, and their results will be compared with experimental results in Sec. IV.

Looking at the full set of data, the SCI signal integrated over the target region and the ZVH spectra integrated Cu- $K_{\alpha}$  peak were linearly correlated, as shown in Fig. 3(c). This suggests that the Cu did not get hot enough to alter the Cu- $K_{\alpha}$

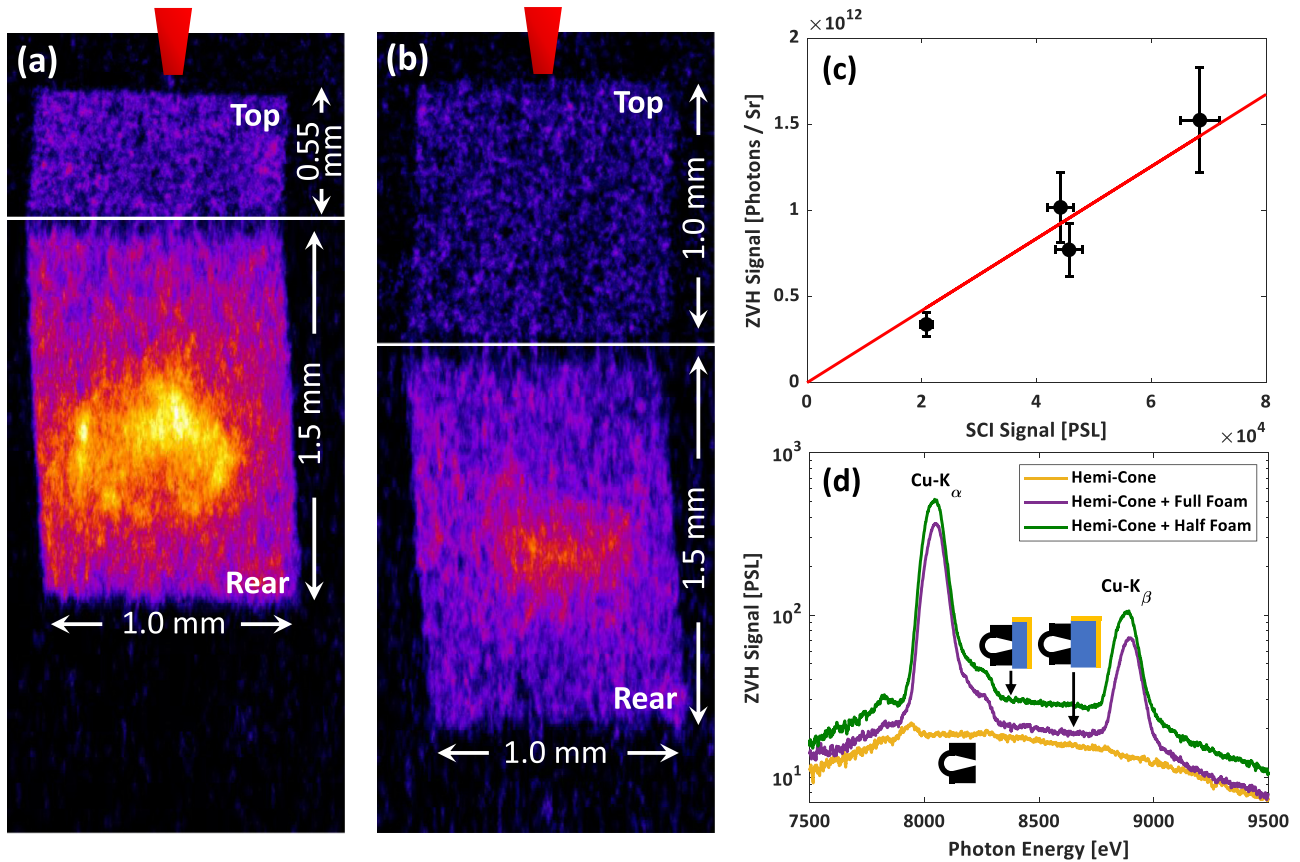


FIG. 3. (a), (b) SCI images of 8.048 keV Cu- $K_{\alpha}$  x-ray emission from Cu foils on the top and rear side of the foam block, with laser depiction (red) to clarify perspective. Two block depths were used to depict x-ray emission profiles at (a) 0.55 mm and (b) 1.0 mm. The signal consists of a relatively uniform background due to scattering energetic electrons and a spot due to forward-directed protons. (c) Linear correlation between the integrated signals from ZVH and SCI, indicating that Cu- $K_{\alpha}$  photon energy did not shift significantly from the cold value. (d) ZVH spectra for various target structures (hemi-cone spectrum has no Cu). Note that the brighter spectrum comes from a target with less Cu, indicating more proton- and electron-induced interactions with the Cu layers.

emission energy outside of the response window of the crystal imager [30]. Figure 3(d) shows the spectra obtained when protons and hot electrons impinge on the Cu foils for the various targets. The base continuum shown for the hemi-cone

target is brought on by hot electrons refluxing in the hemi and cone structures, which still occurs when foam is added. The added continuum from foam targets (green, purple) represents the particles propagating through the Cu end foils, shown in

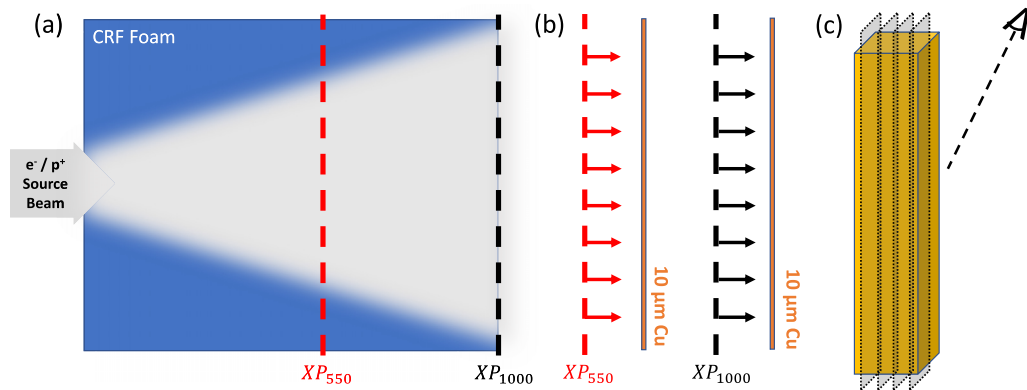


FIG. 4. Multistep simulation strategy to find proton- and electron-induced Cu- $K_{\alpha}$  emission profiles. (a) Protons and electrons are injected and propagate through CRF foam, with extraction planes set at depths of 550  $\mu\text{m}$  and 1000  $\mu\text{m}$ . (b) Extracted particles are then reinjected into 10  $\mu\text{m}$  of Cu, with extraction planes set every  $\mu\text{m}$  in depth. (c) Postprocessing the extracted particles reveals the x-ray emission profile reaching the diagnostic.



gold in the pictograms. Interestingly, the brightest continuum emission (by a factor of 1.5) occurred in the sample with less Cu (2 mm<sup>2</sup> in half foam versus 2.5 mm<sup>2</sup> in full foam), indicating that the number of particles finding their way to Cu was significantly higher in the half-foam target such that it overcame the reduced number of Cu atoms. Because the rear foil emission from the half-foam target has a steep decline at the left and right edges, some particles were likely able to escape through the sides of the foam. The line emission, above continuum, was also greater by a factor of 1.5 for the half-foam case than for the full-foam shot. The reduced emission in the full-foam case is roughly in line with the reduced proton beam energy leaving the target shown in Fig. 2(b).

### III. SIMULATIONS

Simulations of proton transport were carried out to validate the experimental results and investigate the dynamics of intense proton beam transport within the foam. The hybrid fluid-PIC code LSP [31] was used to simulate both energetic protons and electrons moving through the foam, with resulting Cu-K<sub>α</sub> emission calculated through manual postprocessing. LSP uses an implicit algorithm wherein background plasma electrons and ions are simulated as fluid particles, relaxing the space and time resolution requirements to avoid artificial grid heating. This is particularly advantageous for simulating the dense plasmas present in the experiment without resolving plasma oscillations over the long timescale of tens of ps. Grid-based collisional effects in the background species are estimated using the Jones algorithm [32]. The simulation strategy is depicted in Fig. 4. In one set of simulations, kinetic protons and/or hot electrons were injected into a 1 mm foam block. Extraction planes at depths of 0.55 mm (half foam, red) and 1.0 mm (foam rear, black) were set up to collect the position and momentum of all passing particles—see Fig. 4(a). In a second set of simulations, the extracted particles from either depth were reinjected into 10 μm Cu, with extraction planes set up every 1 μm in depth—see Fig. 4(b). Postprocessing of these extraction planes yielded the Cu-K<sub>α</sub> emission according to the particle energies and positions—see Fig. 4(c). We point out that with this strategy, we do not simulate the interface effects between different materials.

In all simulations, the background materials were initialized as ion and electron plasma fluid species with starting temperature  $T_0 = 1$  eV. Based on chemical analysis, the CRF foam had composition like C<sub>12</sub>H<sub>4</sub>O; it was simulated as a single fluid ion species with density  $1.4 \times 10^{21}$  cm<sup>-3</sup>, with complementing electron fluid species. Calculations of the electron collision frequencies within the foam target with this initialization were dubious, so electromagnetic field advancement was switched off. We note that previous simulations with similar current densities showed insignificant differences in proton transport when fields were switched on or off, which may justify this omission of fields. Cu ions were also initialized as a fluid plasma with density  $8.5 \times 10^{22}$  cm<sup>-3</sup>. The charge state of Cu ions was determined by Prism's PrOpacEOS [33] based on the local density and temperature. The energy deposition and scattering of kinetic proton and hot electron species into the foam are governed by a Monte Carlo approach within the dEdx module using present values

of the local target thermodynamic state as in Ref. [34]. Energy deposition into Cu is governed by an advanced dynamic proton stopping power module [15], wherein the bound and free electron contribution to stopping power are added together based on the charge state.

#### A. Protons' source treatment

To reconstruct the proton beam incident on the foam, we use the proton energy spectrum measured from RCF data corresponding to the hemi-cone structure. This is modeled as a Maxwellian  $dN/dE \propto \exp(-E/T_p)$  with characteristic beam temperature  $T_p = 6.1$  MeV. The beam energy incident on the RCF was 4.16 J, but given the small solid angle subtended by RCF 16 cm behind the target, this is less than the actual total beam energy. When compared with previous experiments using similar target structures and short-pulse laser parameters [7], the total beam energy is scaled up to 14 J. See Sec. VI for more details. We also assume an approximately Gaussian current density profile  $J(x) = J_0 \exp(-x^2/\sigma^2)$  [35] with on-foam beam radius  $\sigma = 45$  μm. The current density is cut off to zero for  $x > 100$  μm corresponding to the cone's opening radius through which protons enter the foam. Combining the Maxwellian spectrum, total beam energy, Gaussian profile, and beam pulse 10 ps to mimic the Omega-EP laser pulse duration, the peak current density is calculated as  $J_0 = 3.6 \times 10^9$  A/cm<sup>2</sup>. Using these fundamental inputs for the beam, we can implement beam divergence in two ways, described in the following paragraphs, using transverse thermal distributions.

From previous simulations used in Ref. [7], we gather a single transverse thermal distribution with  $T_{\perp} = 105$  keV, corresponding to the divergence of the outgoing beam from the cone structure. Note that this *transverse* temperature is independent of the aforementioned *longitudinal* temperature  $T_p$  used in the Maxwellian energy spectrum  $dN/dE$ . We will call the above proton beam implementation the single-injection (SI) source, since all the parameters described above are encompassed in a single proton source injection.

It has been shown, however, that TNSA protons exhibit a nontrivial energy-dependent maximum divergence [1,36]. The half-opening angle of the lowest energy protons is typically around 25°-30°, and that of the highest energy protons is 6° or lower. In between, a parabolic fit can be used to match experimental data [36,37], represented here as  $\theta_{\max}(E)$ . We implement this energy dependence by splitting the beam into multiple injections, each covering a different bin of proton energies. A transverse temperature  $T_i^{\perp}$  can then be individually assigned to each *i*th injection that determines the approximate opening angle for that injection. This implementation can be used for any  $\theta_{\max}(E)$  empirically found from experiments; this work utilizes that found in Ref. [37]. We will call this beam implementation the multi-injection (MI) source. Note that the fundamental beam parameters described in the first paragraph of this section are still utilized in the MI source. More technical details can be found in Sec. VI.

A comparison of the SI and MI source implementations is shown in Fig. 5. Figures 5(a) and 5(c) depict the dispersion of the SI and MI sources, respectively, by distinguishing the particle energy map 10 ps after injection. The lines approximate the opening angle trajectory of the lowest (purple) and

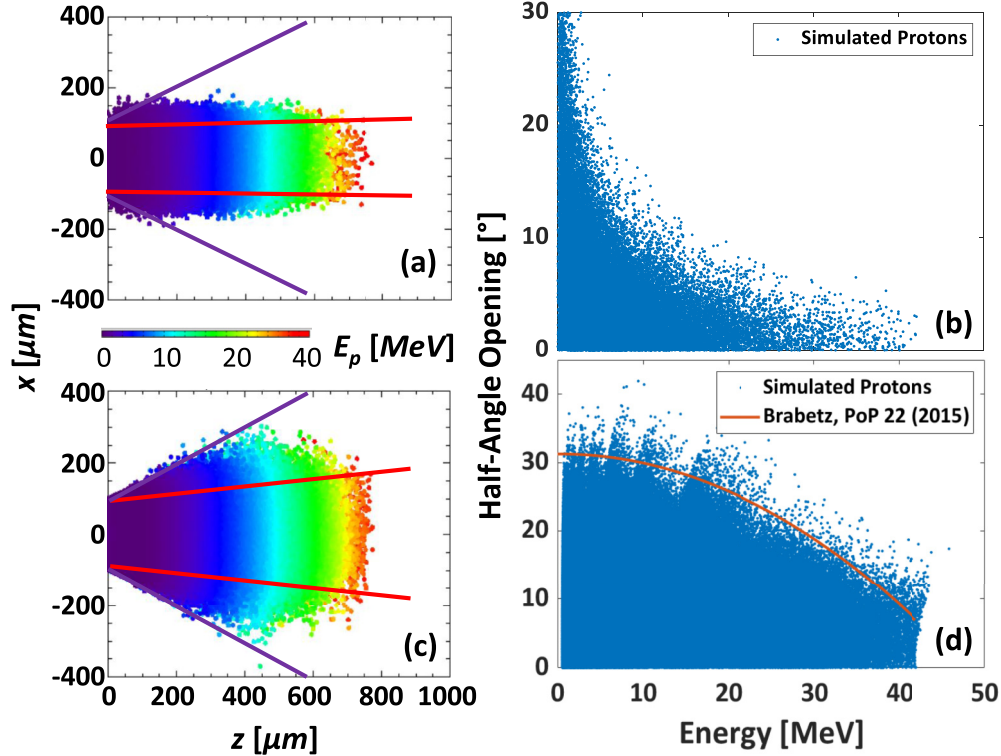


FIG. 5. Comparison of SI and MI source injections into vacuum. (a), (c) Proton energy maps 10 ps after injection for the SI and MI sources, respectively. (b), (d) Particle energy dependence of maximum half-opening angle for the SI and MI sources, respectively. In (d), the empirically measured half-angle opening curve is overlaid for comparison.

highest (red) energy protons. For the SI source, albeit there is a difference in opening angle, it is seen more blatantly with lower energy protons. The red lines are almost parallel, indicating that the opening angle is negligible for high-energy protons, which is not necessarily seen experimentally. The highest energy protons' opening angle in the MI source, however, is non-negligible, conforming with past experiments. Figures 5(b) and 5(d) are the corresponding scatter plots of the opening angle versus particle energy for the SI and MI sources. Even though the plot is saturated at low energies and low angles, the upper bound of the half-opening angle as a function of particle energy defines the correspondence to  $\theta_{\max}(E)$ . Whereas the SI source has a concave, almost hyperbolic  $\theta_{\max}(E)$ , the MI source more accurately follows the empirically found parabolic profile of  $\theta_{\max}(E)$ . Thus, we can more accurately simulate the proton beam energy spread (and therefore the energy deposition) with the MI source.

Note that  $\theta_{\max}(E)$  from a hemi-cone structure likely differs with that from a flat foil; Simulations have shown that even when the cone structure successfully reduces the proton beam radius, the laser intensity and cone tip material have a significant effect on the beam divergence after the tip, altering  $\theta_{\max}(E)$  substantially [35]. In extreme cases, proton beam hollowing can occur due to the strong magnetic fields generated at the cone tip.

### B. Electrons' source treatment

Hot electrons resulting from the laser interaction with the hemi were also implemented to evaluate their contribution to

Cu- $K_{\alpha}$  generation. The hot electron source was taken from simulations similar to those in Ref. [7] (hemi cone), with the primary exception being laser energy (target structure and other laser parameters were identical). Kinetic electrons were extracted at the end of the cone and, in a separate simulation, reinjected into the foam. These simulated hot electrons had source radius  $100 \mu\text{m}$ , total particle count  $1.3 \times 10^{15}$ , and duration 40 ps. They exhibited a Maxwellian distribution with temperature  $T_h \approx 2 \text{ MeV}$  and a large initial divergence (half-opening angle  $\sim 50^\circ$ ) that will be important for the resulting Cu- $K_{\alpha}$  profiles.

### C. Simulation results: Transport and heating

The results of the proton and electron transport simulations are shown in Fig. 6, at various times of transport. The simulations were run for 75 ps to allow ample time for most protons (with enough energy to significantly induce Cu- $K_{\alpha}$  emission) to reach the extraction planes at 0.55 mm and 1.0 mm. Figure 6(a) shows the proton beam density and induced electron temperature within the foam. The protons' trajectories are mostly ballistic, suggesting that the incident angles at which protons are injected are mostly conserved in their transport through the foam. Indeed, compared to solid density, the low density of the foam reduces the collision frequency significantly, in turn reducing the scattering of the protons.

Interestingly, Fig. 6(b) shows the foam electron population reaching temperatures up to several keV, corresponding to the energetic protons' energy deposition. At higher divergence angles and/or greater depths in the foam, the temperature peaks

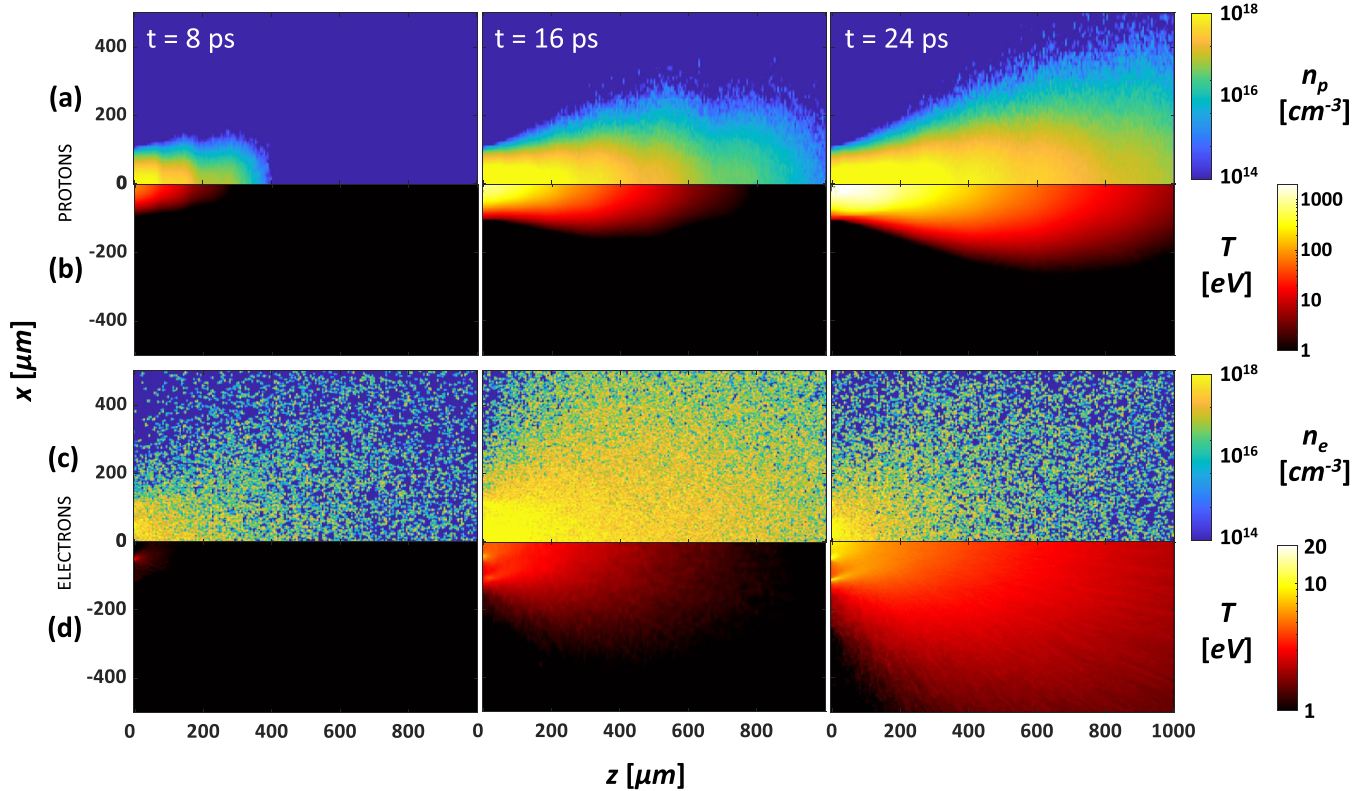


FIG. 6. Simulation results of proton (a) and electron (b) transport through plastic foam target at three delays  $t = 8, 16,$  and  $24$  ps relative to laser irradiation of the hemi. Particle densities (sub-top) and the resulting foam electron temperatures (sub-bottom) show that protons are able to heat the foam more than kinetic electrons by at least an order of magnitude.

at several hundreds of eV. This is likely due to the energy-dependent beam divergence implementation, as explained in Sec. III A. Because the transverse velocity distribution is Gaussian for all particles, the majority of particles will still be propagating longitudinally, so most of the deposited energy will still be longitudinal, with a smooth falloff in the transverse direction. Protons with energy below 5 MeV will deposit all of their energy within 1 mm and stop within the foam. Because the overall temperature of the proton beam is 6 MeV, there will be a substantial amount of protons depositing their energy at half angles of  $20 - 30^\circ$ .

The results of the hot electron transport simulation are shown in Figs. 6(c) and 6(d), also at three different times of transport. Recall that these hot electrons originate from the laser-hemi interaction in a previous simulation, and the effects of that simulation are imprinted in the foam simulations here. For example, the line of electron heating visible in Fig. 6(d) at  $z = 0$ ,  $|x| \approx 110 \mu\text{m}$  is due to a significant population of hot electrons that traveled through the cone bulk along its surfaces before entering the foam. These hot electrons mostly retain their high energies and are able to induce Cu- $K_\alpha$  emission at both depths of Cu. The increased electron density for  $|x| < 100 \mu\text{m}$  represents both hot electrons directed forward into the cone vacuum early as well as electrons copropagating with the protons.

#### D. Postprocessing for Cu- $K_\alpha$ profiles

The extraction planes set in  $\delta z$  spacing within the Cu recorded the position and momentum (and therefore en-

ergy) of all proton/electron particles traversing Cu foils. To calculate the Cu- $K_\alpha$  emission profile due to these particle collisions, we compute the total ionization cross section by summing the individual cross section per particle according to their energies [38,39] and binning them in  $x$  to obtain the transverse profile  $\Delta\sigma(x)$ . Assuming the particle energy remains approximately constant over the spacing between extraction planes  $\delta z$ , the total Cu- $K_\alpha$  yield is  $n\Delta\sigma(x)\delta z$ . In addition, the total yield must be reduced according to (1) the solid angle collected by the SCI and (2) the opacity of Cu. Since the spherical crystal is sufficiently far from the foam block covering a small solid angle, the angle of emission ( $27^\circ$ ) can be treated as constant. The amount of Cu through which photons pass, however, depends on which extraction plane they originate, i.e., the extraction planes closer to the Cu rear travel through less Cu. Taken together, the total emission density can be expressed as

$$\frac{dY_{K\alpha}}{dx} = \sum_{i=0}^9 \left[ \frac{d\sigma}{dx} \right]_i n \delta z e^{-\kappa_v \rho L(i)}, \quad (1)$$

where  $\kappa_v$  is the mass attenuation coefficient of Cu at photon energy  $h\nu = 8.048$  keV, and  $n$  and  $\rho$  are the number and mass density of Cu, respectively.  $L(i) = (10 \mu\text{m} - i\delta z) / \sin(27^\circ)$  is the length of Cu that photons from the  $i$ th extraction plane pass through, and  $\delta z = 1 \mu\text{m}$  spacing.

Energy conservation among the particles and fluids is held during the simulations, with the primary transfer of energy being proton energy deposition given to the background



electrons and ions. However, as the Cu- $K_{\alpha}$  calculations were performed in postprocessing, the radiated energy loss was not represented during the simulation. From the particle data collected in the simulations of transport in copper and calculated emission based on cross sections, we find that the total energy conversion efficiency from beam protons to Cu- $K_{\alpha}$  x rays is 0.5%, and that from beam electrons is 1.0%. This means that the Cu- $K_{\alpha}$  radiation was not a significant loss and energy was therefore approximately conserved.

#### IV. DISCUSSION

Since the target cone structure is in direct contact with the cone bulk, hot electrons have yet another means of escape. These electrons not only have a wide divergence beyond the cone due to enhanced magnetic fields at the cone tip [35], but also scatter relatively quickly throughout the low-density foam. Both of these attributes contribute to the approximate uniformity of the electron population at the top Cu foil. This is confirmed in our 2D simulations of hot electron transport through foam in Fig. 6(b). While the electron population is nonuniform near the foam front, they diverge and scatter quickly enough to uniformly populate the top (and bottom) of the foam. It should be noted that the foam height was larger in the experiment than what was simulated, which would only make the electrons reaching the top foil more uniform.

Crucially, hot electron simulations through foam also show that the population is relatively uniform at foam depth 1 mm. The central bright spots on the foam rear, therefore, must at least partially be due to the proton beam. This is confirmed in our 2D simulations of proton beam transport through the foam in Fig. 6(a). There are orders of magnitude fewer (if any) protons reaching the top of the foam compared to the rear, leaving the uniform population of electrons noted above. On the foam rear, there is a densely populated central region of protons that decays radially, matching the experimental x-ray emission profile.

The postprocessed Cu- $K_{\alpha}$  radial emission profiles at both foam depths are displayed in Fig. 7, calculated as described in Sec. III D. At both 0.55 mm and 1 mm depths, hot electron-driven emission is significant at large radii and exhibits a gradual incline toward the center. Proton-driven emission, on the other hand, is primarily on axis and drives up the centralized total emission profile (solid curve). This sheds light on the qualitative features within the SCI images in Fig. 3. The half-foam target [Fig. 3(a)] exhibits a more pronounced central peak—visually by a sharp change in gradient around  $r = 250 \mu\text{m}$ —compared to the full-foam target [Fig. 3(b)]. Simulations show that this may be attributed to protons whose emission is confined to  $r = 250 \mu\text{m}$ , whereas electron emission is gradual up to  $r = 500 \mu\text{m}$ . This indicates that the protons retained their beamlike qualities experimentally.

The qualitative match between simulations and experiment suggests that the proton beam propagates without filamenting through the low-density foam. An additional simulation was run with electromagnetic field calculations switched on, and only small magnetic fields ( $\sim 10 T$ ) were observed with no noticeable effects on proton beam transport. This is because space-charge effects do not play an important role since the beam is neutralized by the relatively high density

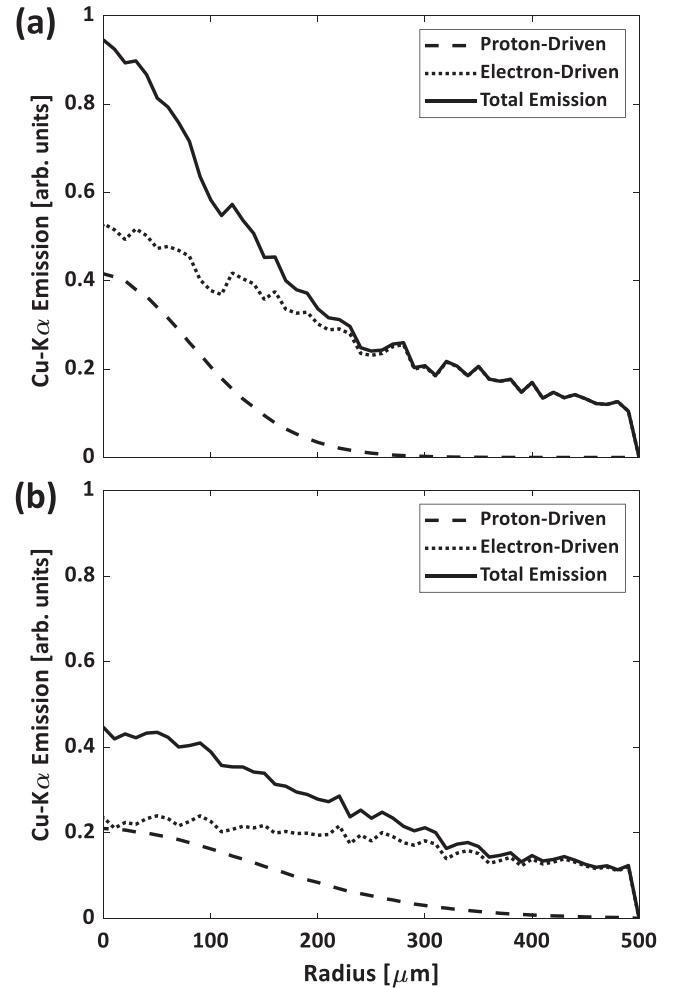


FIG. 7. Cu- $K_{\alpha}$  radial emission profiles from post-processing of simulations of 0.55 mm (a) and 1.0 mm (b) foam depths. Arbitrary units refer to the same scale, resulting in a peak on-axis emission at the half foam greater than that in the full foam by a factor of 2. At both depths, the total emission profile (solid curve) is subdivided into its component electron-driven (dotted curve) and proton-driven (dashed curve) emissions.

of background electrons compared to protons. The resulting low resistive magnetic field is reasonable if we consider the current density gradient. With peak current density  $J_0 \sim 10^9 \text{A/cm}^2$  and beam transverse scale length  $\gtrsim 100 \mu\text{m}$ , the current density gradient is not significant enough to generate a focusing magnetic field [15]. Simulations have shown, however, that decreasing the cone tip diameter can further focus proton beams [7], presumably up to a limit. Proton beam requirements for FI include total beam energy tens of kJ (with Maxwellian temperature several MeV) fit into a spot size of  $\sim 20 \pm 10 \mu\text{m}$  on the compressed core. To achieve this, the peak proton current density must be orders of magnitude larger than what was attained in this experiment, which begets much steeper current density gradients. At these levels, self-generated magnetic fields will almost certainly affect the transport of the beam through a coronal plasma. Whether the fields act to self-consistently focus or defocus the beam depends on a number of properties of the transport



medium as well as beam stopping power. Efforts to mitigate unstable transport effects or use them to our advantage (i.e., focus the beam) must be investigated experimentally, analytically, and computationally to best determine the prospects of proton FI.

Honrubia and Murakami [40] explored the effects of proton beam divergence (beyond the cone) on proton FI requirements, yet the beam model assumes that a proton's deflection angle after the cone was chosen at random, while within a fixed beam divergence. The randomized deflection angle does not take into account the energy-dependence of beam divergence, i.e., higher energy protons are more likely to have a lower deflection angle. Nevertheless, they determined that proton beams with diameter 20-30  $\mu\text{m}$  and divergence half angle below  $10^\circ$  have minimum ignition energy below 20 kJ (assuming the beam is injected  $\sim 90 \mu\text{m}$  away from the compressed core). Temporal *et al.* determined that the proton bandwidth 7-19 MeV was crucial to ignition from a proton beam with temperature  $T_p = 3 \text{ MeV}$  and diameter 20  $\mu\text{m}$  at the compressed core. Our analysis shows that the divergence of a particular bandwidth of protons may actually be less than the total divergence of the beam. Given a fixed overall beam divergence, confining the crucial bandwidth of the proton beam to the necessary divergence may further relax the proton beam intensity requirements. In our analysis, the 7-19 MeV proton bandwidth still has a divergence half angle between  $25^\circ$  and  $30^\circ$ , but further experimental and/or computational work is necessary to explore the energy dependence of proton beam divergence beyond cone structures.

More recent work [41] has shown interesting effects of self-generated fields in hemi-cone targets. In hemi-cone structures with open cone tips, high-energy protons ( $> 30 \text{ MeV}$ ) exhibit an annular profile, while lower energy protons appear focused in the region that would otherwise be within the annulus. This was not observed with a hemi-cone structure with a closed tip. A possible explanation was that transverse electric fields generated near the open cone tip overfocused the highest energy protons which arrived early in time. At later times, some combination of a decaying electric field and lower energy protons arriving did not produce an annular effect. In the case of this work, because the foam block was in direct contact with the cone, one may argue that it was analogous to an enlarged cone tip, in which case an annular effect would not have been observed. Nevertheless, proton FI studies [20] have shown that, given the necessary beam energy, the proton spectral window primarily responsible for ignition is between 7 and 19 MeV for a compressed core with density  $625 \text{ g/cm}^3$ . Since the highest energy protons are outside this range, the annular effect may not be detrimental to ignition success. That being said, it would be interesting to find the foam (plasma) density below which this annular profile effect starts to appear, and which parameters increase or decrease the proton energy threshold at which the annular effect occurs.

The foam temperature evolution observed in simulations due to proton energy deposition is also unexpectedly high. Analogous simulations were performed with the exact same proton source model, but using solid aluminum ( $\rho = 2.7 \text{ g/cm}^3$ ) and vitreous carbon foam (with identical  $\rho_{\text{foam}} = 0.38 \text{ g/cm}^3$ ) instead of the foam. In these alternate material cases, the temperature map had the same characteristic con-

tours as in Fig. 6(a), which was expected given the energy deposition and beam divergence. In the case of vitreous carbon foam, the fluid electron temperature still reached several keV, while that in Al reached a maximum of 150 eV, which is consistent with previously run simulations with roughly similar beam parameters.

One possible explanation for the exorbitant temperatures is as follows. At least in metals at high temperatures ( $\gtrsim T_{\text{Fermi}} \sim \text{eV}$ ), the electron heat capacity is modeled as an ideal gas of free electrons, i.e.,  $du/d(k_B T) \propto n_f$ . Because the density of the foam is about ten times lower than that of Al, the heat capacity of the foam could also be proportionately lower. This means it takes far less energy to change the temperature of the foam by an arbitrary degree than it does to change the temperature of Al by the same degree. Even when SRIM calculations [42] show that peak stopping power in Al is 4x that in CRF foam (i.e., the energy deposited in Al is 4x greater than that deposited in the foam), the order of magnitude difference in density (and heat capacity) outweighs the stopping power calculations. We should note that these simulations can be made more accurate with better equation-of-state modeling of plastics. Since the material spends very little time in the cold solid regime, we can neglect those heat capacity models.

## V. CONCLUSIONS

In summary, we conducted an experiment which directed the proton beam from a typical TNSA hemi-cone configuration into CRF foam with thickness 0.55 or 1.00 mm with a rear Cu layer to study transport of the intense beam. The addition of a massive cone to the target hemi foil reduced the total beam energy by 50% and reduced the Maxwellian temperature by over 50%. Images of x-ray emission show a bright spot on the rear Cu film indicative of a forward-directed beam without major breakup. Simulations of the transport were conducted using a multi-injection proton source with the experimentally obtained energy spectrum but with energy-dependent angular spread. The modeling included contributions from hot electrons which broadly filled the foam. Synthetic Cu- $K_\alpha$  maps were generated through an additional simulation step and post-processing. While hot electrons produce an emission profile gently declining with radius, protons produce a centralized emission profile which drives up the emission on axis, in qualitative agreement with experiment. This suggests that protons retain their beamlike qualities well into the low-density plasma. Simulations also showed that the intense, cone-focused proton beam was able to heat the low-density foam to temperatures above 1 keV, which could be important for future studies if verified experimentally.

The proton current densities generated in this experiment were not intense enough to induce significant magnetic fields within the foam, but future work includes assessing the proton transport dynamics of more intense beams through metal blocks. Proton beams can be made more intense by increasing the cone half angle and/or reducing the tip radius, among other methods. Current calculations predict that several tens of kJ in proton beam energy must be compacted into several tens of  $\mu\text{m}$  diameter to successfully ignite a typical DT capsule. At

these scales, developing analytic models to predict collective effects on proton beam transport will be crucial.

## VI. METHODS

Regarding the analysis of the RCFs, because of the long standoff distance, only a portion of the beam was intercepted by the first several layers in each pack. The fit temperature and energy presented in Fig. 2(b) include only what intercepted the packs and fit to data beyond the first layer. The whole proton beam, therefore should have a representative temperature that is lower (we estimate only slightly lower) than the fit value, while the total beam energy is considerably higher than the presented values. To estimate the full energy of the beam, we employed a data set taken in a different shot day with hemi targets and RCF with standoff only  $\sim 8$  cm. In that data set, at each of the layer energies, a ratio was found of the total dose divided by the dose contained in the square cone corresponding to this experiment, and the present data set was weighted accordingly. The proton transport simulations (see Sec. III) were based on this full extrapolated energy and the fit temperature. N.B. the films were scanned before the recent refined scanning techniques presented in Ref. [43] and are no longer viable.

Regarding the MI source implementation, assigning a transverse temperature amounts to implementing a Gaussian transverse velocity distribution

$$dN/dv_{\perp} \propto \exp(-v_{\perp}^2/v_{\text{th}}^2), \quad (2)$$

where  $v_{\text{th}}^2 = 2T_{\perp}/m$  with (proton) mass  $m$ . With this setup, a transverse temperature  $T_{i}^{\perp}$  corresponding to the maximum opening angle for the  $i$ th injection (representing the longitudinal energy bin  $E_i \leq E < E_{i+1}$ ) can be determined in the following way. The maximum half-opening angle of an injection is determined by the maximum transverse velocity and the minimum longitudinal velocity in that injection. Since the transverse velocity distribution [Eq. (2)] is Gaussian,  $v_{\perp}$  substantially (by 98%) decays by  $v_{\perp} = 2v_{\text{th},i}^{\perp}$ —this can be used as an approximate maximum transverse velocity. The minimum longitudinal velocity is determined by the lower limit of the energy bin  $v_i = \sqrt{2E_i/m}$ . The maximum half-opening angle is then  $\theta_{\text{max}} \approx \tan^{-1}(2v_{\text{th},i}^{\perp}/v_i) = \tan^{-1}(2\sqrt{T_{i}^{\perp}/E_i})$ . Here we assume nonrelativistic protons. The transverse temperature

is then determined by matching this with the parabolic fit  $\theta_{\text{max}}(E_i)$ :

$$T_{i}^{\perp} = \frac{E_i}{4} \tan^2(\theta_{\text{max}}(E_i)). \quad (3)$$

It must also be ensured that an injection's *minimum* half-opening angle does not stray far from  $\theta_{\text{max}}(E)$ . The minimum half-opening angle is governed by an injection's upper energy limit  $E_{i+1}$  (also the lower limit of the proceeding energy bin). Given the lower energy limit  $E_i$  and transverse temperature  $T_{i}^{\perp}$  of an injection, the upper energy limit  $E_{i+1}$  can be determined by comparing the half-opening angle of the  $i$ th injection's *highest* energy protons  $\theta = \tan^{-1}(2v_{\text{th},i}^{\perp}/v_{i+1}) = \tan^{-1}(2\sqrt{T_{i}^{\perp}/E_{i+1}})$  with the maximum half-opening angle predicted by  $\theta_{\text{max}}(E_{i+1})$ :

$$\delta\theta = \theta_{\text{max}}(E_{i+1}) - \tan^{-1}\left(2\sqrt{\frac{T_{i}^{\perp}}{E_{i+1}}}\right). \quad (4)$$

In this way, the energy bins can be deduced recursively, starting from the minimum proton beam energy and ending when the maximum proton energy is reached. For these simulations,  $5^{\circ}$  is used as a threshold of  $\delta\theta$ , i.e., the maximum half-opening angle is approximately within  $5^{\circ}$  of  $\theta_{\text{max}}(E)$ , empirically taken from Ref. [37].

The data relevant to this study are available upon reasonable request to the corresponding author.

## ACKNOWLEDGMENTS

This material is based upon work supported by the U.S. Department of Energy National Nuclear Security Administration under the National Laser User Facility program with Award No. DE-NA0002034, the Laboratory Basic Science program, and the High Energy Density Laboratory Plasmas program with Award No. DE-NA0003876. The support of DOE does not constitute an endorsement by DOE of the views expressed in this paper. The authors would like to acknowledge excellent support provided by the Omega EP Laser Facility staff and development effort for the foam targets by General Atomics.

W.T., C.M., and O.D. designed the experiment with help from P.N.M., M.S.W., F.N.B., Y.P., H.S.M., P.K.P., and M.R. K.B. performed the simulations; J.K. and M.E.F. provided computational guidance. A.H., O.D., and C.M. contributed to the data analysis. K.B. and C.M. led the writing of the paper.

The authors declare no competing financial interests.

- 
- [1] R. A. Snavely, M. H. Key, S. P. Hatchett, T. E. Cowan, M. Roth, T. W. Phillips, M. A. Stoyer, E. A. Henry, T. C. Sangster, M. S. Singh, S. C. Wilks, A. MacKinnon, A. Offenberger, D. M. Pennington, K. Yasuike, A. B. Langdon, B. F. Lasinski, J. Johnson, M. D. Perry, and E. M. Campbell, *Phys. Rev. Lett.* **85**, 2945 (2000).
- [2] P. K. Patel, A. J. Mackinnon, M. H. Key, T. E. Cowan, M. E. Ford, M. Allen, D. F. Price, H. Ruhl, P. T. Springer, and R. Stephens, *Phys. Rev. Lett.* **91**, 125004 (2003).
- [3] M. Roth, I. Alber, V. Bagnoud, C. R. D. Brown, R. Clarke, H. Daido, J. Fernandez, K. Flippo, S. Gaillard, C. Gauthier,

- M. Geissel, S. Glenzer, G. Gregori, M. Günther, K. Harres, R. Heathcote, A. Kritcher, N. Kugland, S. LePape, B. Li *et al.*, *Plasma Phys. Controlled Fusion* **51**, 124039 (2009).
- [4] D. Hoarty, T. Guymer, S. James, E. Gumbrell, C. Brown, M. Hill, J. Morton, and H. Doyle, *High Energy Density Phys.* **8**, 50 (2012).
- [5] A. McKelvey, G. Kemp, P. Sterne, A. Fernandez-Panella, R. Shepherd, M. Marinak, A. Link, G. Collins, H. Sio, J. King *et al.*, *Sci. Rep.* **7**, 7015 (2017).
- [6] K. Bhutwala, M. Bailly-Grandvaux, J. Kim, M. Dozieres, E. Galtier, C. B. Curry, M. Gauthier, E. Cunningham, H. J. Lee,

- P. Forestier-Colleoni, A. Higginson, N. Aybar, R. Hua, B. C. Edgill, J. Strehlow, G. M. Dyer, S. H. Glenzer, J. B. Kim, N. Alexander, E. D. Rio *et al.*, *IEEE Trans. Plasma Sci.* **48**, 2751 (2020).
- [7] C. McGuffey, J. Kim, M. S. Wei, P. M. Nilson, S. N. Chen, J. Fuchs, P. Fitzsimmons, M. E. Foord, D. Mariscal, H. S. McLean, P. K. Patel, R. B. Stephens, and F. N. Beg, *Sci. Rep.* **10**, 9415 (2020).
- [8] A. J. Mackinnon, P. K. Patel, M. Borghesi, R. C. Clarke, R. R. Freeman, H. Habara, S. P. Hatchett, D. Hey, D. G. Hicks, S. Kar, D. G. Hicks, S. Kar, M. H. Key, J. A. King, K. Lancaster, D. Neely, A. Nikkro, P. Norreys, M. M. Notley, T. H. Phillips, L. Romagnani, R. A. Snavely, R. B. Stephens, and R. P. J. Town, *Phys. Rev. Lett.* **97**, 045001 (2006).
- [9] J. Cobble, R. Johnson, T. Cowan, N. Renard-Le Galloudec, and M. Allen, *J. Appl. Phys.* **92**, 1775 (2002).
- [10] L. Gao, H. Ji, G. Fiksel, W. Fox, M. Evans, and N. Alfonso, *Phys. Plasmas* **23**, 043106 (2016).
- [11] M. Roth, T. E. Cowan, M. H. Key, S. P. Hatchett, C. Brown, W. Fountain, J. Johnson, D. M. Pennington, R. A. Snavely, S. C. Wilks, K. Yasuike, H. Ruhl, P. Pegoraro, S. V. Bulanov, E. M. Campbell, M. D. Perry, and H. Powell, *Phys. Rev. Lett.* **86**, 436 (2001).
- [12] J. Fernández, B. Albright, F. N. Beg, M. E. Foord, B. Hegelich, J. Honrubia, M. Roth, R. Stephens, and L. Yin, *Nucl. Fusion* **54**, 054006 (2014).
- [13] R. Roycroft, P. Bradley, E. McCary, B. Bowers, H. Smith, G. Dyer, B. Albright, S. Blouin, P. Hakel, H. Quevedo *et al.*, *Matter Radiat. Extremes* **6**, 014403 (2021).
- [14] A. Kemp, S. C. Wilks, E. Hartouni, and G. Grim, *Nat. Commun.* **10**, 1 (2019).
- [15] J. Kim, C. McGuffey, B. Qiao, M. S. Wei, P. E. Grabowski, and F. N. Beg, *Phys. Plasmas* **23**, 043104 (2016).
- [16] S. C. Wilks, A. B. Langdon, T. E. Cowan, M. Roth, M. Singh, S. Hatchett, M. H. Key, D. Pennington, A. MacKinnon, and R. A. Snavely, *Phys. Plasmas* **8**, 542 (2001).
- [17] J. S. Green, V. M. Ovchinnikov, R. G. Evans, K. U. Akli, H. Azechi, F. N. Beg, C. Bellei, R. R. Freeman, H. Habara, R. Heathcote *et al.*, *Phys. Rev. Lett.* **100**, 015003 (2008).
- [18] J. J. Honrubia and J. Meyer-ter Vehn, *Plasma Phys. Controlled Fusion* **51**, 014008 (2008).
- [19] S. N. Chen, S. Atzeni, T. Gangolf, M. Gauthier, D. P. Higginson, R. Hua, J. Kim, F. Mangia, C. McGuffey, J.-R. Marquès *et al.*, *Sci. Rep.* **8**, 1 (2018).
- [20] M. Temporal, J. J. Honrubia, and S. Atzeni, *Phys. Plasmas* **9**, 3098 (2002).
- [21] S. Atzeni, M. Temporal, and J. Honrubia, *Nucl. Fusion* **42**, L1 (2002).
- [22] X. Vaisseau, A. Morace, M. Touati, M. Nakatsutsumi, S. D. Baton, S. Hulin, P. Nicolai, R. Nuter, D. Batani, F. N. Beg, J. Breil, R. Fedosejevs, J. L. Feugeas, P. Forestier-Colleoni, C. Fourment, S. Fujioka, L. Giuffrida, S. Kerr, H. S. McLean, H. Sawada, V. T. Tikhonchuk, J. J. Santos, *Phys. Rev. Lett.* **118**, 205001 (2017).
- [23] K. Mima, J. Fuchs, T. Taguchi, J. Alvarez, J. Marquès, S. Chen, T. Tajima, and J. Perlado, *Matter Radiat. Extremes* **3**, 127 (2018).
- [24] S. N. Chen, M. Gauthier, M. Bazalova-Carter, S. Bolanos, S. Glenzer, R. Riquier, G. Revet, P. Antici, A. Morabito, A. Propp, M. Starodubtsev, and J. Fuchs, *Rev. Sci. Instrum.* **87**, 073301 (2016).
- [25] T. J. Bartal, Investigation of proton focusing and conversion efficiency for proton fast ignition, Ph.D. thesis, University of California, San Diego, 2012.
- [26] C. Stoeckl, G. Fiksel, D. Guy, C. Mileham, P. Nilson, T. Sangster, M. Shoup III, and W. Theobald, *Rev. Sci. Instrum.* **83**, 033107 (2012).
- [27] L. C. Jarrott, M. S. Wei, C. McGuffey, F. N. Beg, P. Nilson, C. Sorce, C. Stoeckl, W. Theobald, H. Sawada, R. Stephens *et al.*, *Rev. Sci. Instrum.* **88**, 043110 (2017).
- [28] T. Bartal, M. E. Foord, C. Bellei, M. H. Key, K. A. Flippo, S. A. Gaillard, D. T. Offermann, P. K. Patel, L. C. Jarrott, D. P. Higginson, M. Roth, A. Otten, D. Kraus, R. B. Stephens, H. S. McLean, E. M. Giraldez, M. S. Wei, D. C. Gautier, and F. N. Beg, *Nat. Phys.* **8**, 139 (2012).
- [29] B. Qiao, M. E. Foord, M. S. Wei, R. B. Stephens, M. H. Key, H. McLean, P. K. Patel, and F. N. Beg, *Phys. Rev. E* **87**, 013108 (2013).
- [30] K. U. Akli, M. H. Key, H. K. Chung, S. B. Hansen, R. R. Freeman, M. H. Chen, G. Gregori, S. Hatchett, D. Hey, N. Izumi, J. King, J. Kuba, P. Norreys, A. J. Mackinnon, C. D. Murphy, R. A. Snavely, R. B. Stephens, C. Stoeckel, W. Theobald, and B. Zhang, *Phys. Plasmas* **14**, 023102 (2007).
- [31] D. R. Welch, D. V. Rose, M. E. Cuneo, R. B. Campbell, and T. A. Mehlhorn, *Phys. Plasmas (1994-present)* **13**, 063105 (2006).
- [32] M. E. Jones, D. S. Lemons, R. J. Mason, V. A. Thomas, and D. Winske, *J. Comput. Phys.* **123**, 169 (1996).
- [33] Prism Computational Sciences, Inc..
- [34] J. Kim, B. Qiao, C. McGuffey, M. S. Wei, P. E. Grabowski, and F. N. Beg, *Phys. Rev. Lett.* **115**, 054801 (2015).
- [35] J. Honrubia, A. Morace, and M. Murakami, *Matter Radiat. Extremes* **2**, 28 (2017).
- [36] M. Roth and M. Schollmeier, Proceedings of the CAS-CERN Accelerator School: Plasma Wake Acceleration **1**, 231 (2016).
- [37] C. Brabetz, S. Busold, T. Cowan, O. Deppert, D. Jahn, O. Kester, M. Roth, D. Schumacher, and V. Bagnoud, *Phys. Plasmas* **22**, 013105 (2015).
- [38] M. G. Pia, G. Weidenspointner, M. Augelli, L. Quintieri, P. Saracco, M. Sudhakar, and A. Zoglauer, *IEEE Trans. Nucl. Sci.* **56**, 3614 (2009).
- [39] C. Hombourger, *J. Phys. B: At., Mol. Opt. Phys.* **31**, 3693 (1998).
- [40] J. Honrubia and M. Murakami, *Phys. Plasmas* **22**, 012703 (2015).
- [41] A. Higginson, Optimisation and control of ion acceleration in intense laser-foil interactions, Ph.D. thesis, University of Strathclyde, 2018.
- [42] J. F. Ziegler, M. D. Ziegler, and J. P. Biersack, *Nucl. Instrum. Methods Phys. Res., Sect. B* **268**, 1818 (2010).
- [43] C. B. Curry, C. A. S. Dunning, M. Gauthier, H.-G. J. Chou, F. Fiuza, G. D. Glenn, Y. Y. Tsui, M. Bazalova-Carter, and S. H. Glenzer, *Rev. Sci. Instrum.* **91**, 093303 (2020).